RSC Advances

PAPER

View Article Online
View Journal | View Issue

Cite this: *RSC Adv.*, 2017, 7, 21145

Selective hydrodeoxygenation of 5-hydroxy-2(5*H*)-furanone to γ-butyrolactone over Pt/mesoporous solid acid bifunctional catalyst†

Bingfeng Chen, Fengbo Li* and Guoqing Yuan*

Received 18th March 2017
Accepted 5th April 2017

DOI: 10.1039/c7ra03205f

rsc.li/rsc-advances

Selective hydrodeoxygenation of 5-hydroxy-2(5*H*)-furanone (HFO) derived from furfural oxidation to γ-butyrolactone (GBL) provides a sustainable alternative to the petroleum-based process for γ-butyrolactone production. Furfural is first converted to HFO through selective photocatalytic oxidation by using air oxygen as the oxidant (yield: 85.0%). HFO is further converted to GBL through hydrodeoxygenation over noble-metal nanoparticles on mesoporous Nb–Zr mixed oxides. The conversion of HFO to GBL involves two reactions: hydrogenation catalyzed by active metal and dehydration over mesoporous solid acids. The catalytic properties of M/Nb–Zr mixed oxides (M = Pt, Ir, Ru, Rh and Pd) are related to the composition of support and active metal. The incorporation of zirconia into matrixes improves the thermal stability of mesoporous mixed oxides and increases the amounts of surface acid, which contributes to its catalytic selectivity to GBL. Pt/Nb_5Zr_5-550 exhibited the best catalytic performances with 97.3% selectivity of GBL at full conversion. The excellent performance can be correlated with the cooperative effect between active metal species and acid sites. The Pt-solid acid bifunctional catalysts show superior catalytic performance compared with conventional catalysts, such as Pt/H-ZSM-5, Pt/C, Rh/C or Pd/C. An overall GBL yield of 82.7% from furfural was obtained.

1. Introduction

γ-Butyrolactone (GBL) is considered as an important C4 feedstock, which can be used as the main intermediate for the synthesis of pyrrolidone and pyrrolidone-derivatives, pharmaceuticals, agrochemicals and rubber additives.[1,2] It can also be used as an eco-friendly solvent or extraction agent in petroleum processing and textile industries.[3] There are several approaches for GBL production, such as hydrogenation of maleic anhydride,[4,5] dehydrocyclization of 1,4-butanediol (BDO),[3,6,7] and hydrogenation of succinic acid or dialkyl succinate.[8–11] The former two methods are based heavily on fossil fuel resources and the last one is derived from succinic acid produced through fermentation of sugars and starches.[12] However, the fermentation process shows the low productivity. More efficient processes based on biomass resources attract great attention during developing novel catalytic pathway for GBL production.

Furfural is the most important platform chemical, which is produced from hemicelluloses through dehydration with an annual production of 5 million tons.[13] Furfural can be applied as a feedstock molecule for the production of GBL through tetrahydrofuran (THF) as an intermediate. Several homogeneous or heterogeneous catalysts have been attempted to oxidation of tetrahydrofuran to GBL.[14–17] Sooknoi *et al.* have applied the thermally treated iron-containing clay catalyst to convert THF into GBL with H_2O_2 as the oxidant and the best yield of GBL was only 16.6%.[18] This conversion has some drawbacks, such as multiple-step reactions (including decarbonylation, hydrogenation and oxidation), low efficiency, and a large investment in equipment. Maleic acid and succinic acid can also be produced through the selective oxidation of furfural and further hydrogenation of them leads to the formation of GBL. There are many catalytic systems for furfural oxidation, such as $H_3PMo_{12}O_{40}/Cu(NO_3)_2$,[19] $H_5PV_2Mo_{10}O_{40}/Cu(CF_3SO_3)_2$,[20] Amberlyst-15/$H_2O_2$,[21] titanium silicalite,[22] and VO_x/Al_2O_3.[23] Homogeneous catalysts show relatively poor selectivity and the separation of the products and the catalysts poses a great problem in practical operation. Heterogeneous processes of furfural oxidation require high reaction temperature and short contact time and the main drawback is the inevitable thermal polymerization of furfural under reaction conditions.[24]

In our work, a sustainable catalytic process for GBL production from furfural is steadily developed *via* a novel intermediate: 5-hydroxy-2(5*H*)-furanone (HFO), as illustrated in Scheme 1. Furfural is first converted to HFO through selective photocatalytic oxidation by using air oxygen as the oxidant. HFO is further converted to GBL through hydrodeoxygenation over

---

Beijing National Laboratory of Molecular Science, Key Laboratory of Green Printing, Institute of Chemistry, Chinese Academy of Sciences, Beijing, 100190, P. R. China. E-mail: lifb@iccas.ac.cn; yuangq@iccas.ac.cn; Fax: +86-10-62559373; Tel: +86-10-62634920

† Electronic supplementary information (ESI) available. See DOI: 10.1039/c7ra03205f

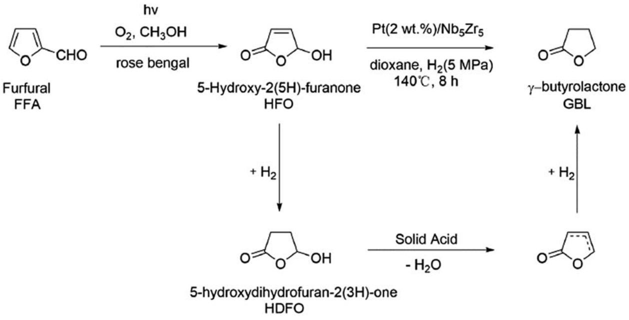

Scheme 1 Catalytic conversion of furfural into γ-butyrolactone.

a bifunctional catalyst under mild conditions. The catalyst is prepared by supporting noble-metal nanoparticles on mesoporous Nb–Zr mixed oxides that are synthesized through a modified evaporation-induced self-assemble (EISA) approach. The physicochemical properties of these materials are detailedly investigated and the reaction conditions of γ-butyrolactone production are optimized. The conversion of HFO to GBL involves two reactions: hydrogenation and dehydration. These reactions can be integrated over one catalyst with bifunctional active sites: Pt nanoparticles for hydrogenation and mesoporous solid acids for dehydration. To the best our knowledge, it is the first time that 5-hydroxy-2(5*H*)-furanone derived from furfural oxidation is smoothly converted into γ-butyrolactone through catalytic hydrodeoxygenation.

2. Experimental

2.1 Chemicals

Triblock copolymer Pluronic P123 (Mw = 5800, $EO_{20}PO_{70}EO_{20}$) and Pluronic F127 (Mw = 12 600, $EO_{106}PO_{70}EO_{106}$) were purchased from Sigma Aldrich Crop. NbCl5, $Zr(OBu)_4$ (80% w/w in 1-butanol), H_2PtCl_6, H_2IrCl_6, $RuCl_3$, $RhCl_3$ and $PdCl_2(CH_3CN)_2$ were purchased from Alfa Aesar. Furfural, rose bengal, methanol, 1-propanol, chloroform, dioxane and THF were obtained from Aladdin Reagent Limited Company (Shanghai, China). Pd(10 wt%)/C, Rh(5 wt%)/C, Pt(5 wt%)/C, Al_2O_3 and ZSM-5 were provided by Strem. All chemicals were used as received. Furfural was used after vacuum distillation.

2.2 Catalysts preparation

Mesoporous Nb_2O_5–ZrO_2 mixed oxides ($Nb_{10-x}Zr_x$-T, x is the Zr/(Nb + Zr) mole ratio and T is the calcination temperature), were synthesized through a modified evaporation-induced self-assemble (EISA) approach. During a typical preparation procedure of Nb_5Zr_5-550, F127 (1.0 g) was dissolved in 1-propanol (10.0 g) by ultrasonic dispersion. $Zr(OBu)_4$ (3.0 mmol, 80% w/w in 1-butanol) and $NbCl_5$ (3.0 mmol) were added to the mixture under stirring. The mixture was stirred vigorously for 2 h at room temperature and then 0.54 g H_2O was added. After being further stirred for 1.0 h, the mixture was transferred to Petri dishes to undergo the slow EISA process at 40 °C for 4–6 days. The as-synthesized xerogel was calcined at 550 °C for 4.0 h in air to remove the structure-directing agents. Mesoporous Nb–Zr oxides with different compositions were synthesized by adjusting the proportions of $Zr(OBu)_4$ and $NbCl_5$ (the total Nb–Zr molar is 6 mmol). The soft template F127 can be replaced by P123.

The supported bifunctional catalysts were prepared by a wet impregnation method. The as-synthesized mesoporous mixed oxides ($Nb_{10-x}Zr_x$-T) were used as support materials. The calculated amount $Nb_{10-x}Zr_x$-T was impregnated with a certain concentration aqueous solution of metal precursors (such as H_2PtCl_6, H_2IrCl_6, $RuCl_3$, $RhCl_3$ and $PdCl_2(CH_3CN)_2$) and kept in an oven at 383 K overnight. Then these solids were calcinated at 400 °C in air for 3.0 h. These catalysts were activated under diluted hydrogen flow (H_2/Ar: 10%) at 400 °C for 2.0 h before catalytic tests. The loading amount of metal is stated as 2 wt%. The metal loadings quoted were confirmed by the ICP-AES elemental analysis. They are in good agreement with the preparation stoichiometries since the preparations did not involve operations such as filtration and washing which could cause metal loss.

Pt/Al_2O_3 and Pt/HZSM-5 catalysts were also prepared by the wet impregnation method. The specified preparation processes of these catalysts were similar to the above-mentioned procedure.

2.3 Materials characterization

Powder X-ray diffraction (XRD) patterns were measured on a Rigaku Rotaflex diffractometer equipped with a rotating anode and a Cu-Kα radiation source (40 kV, 200 MA; $\lambda = 1.54056$ Å). Nitrogen adsorption–desorption analysis was carried out at 77 K on a Quadrasorb SI-MP adsorption analyzer. Before the adsorption analysis, the samples were outgassed under a vacuum at 300 °C in the port of the adsorption analyzer. Inductive coupling plasma emission spectrometer (ICP-OES) analysis was conducted on the Varian 710 ICP-OES with ICP Expert II software. XPS data were obtained with an ESCALab220i-XL electron spectrometer from VG Scientific using 300 W Al-Kα radiations. The base pressure was approximately 3×10^{-9} mbar. The binding energies were referenced to the C 1s line at 284.8 eV from adventitious carbon. The Eclipse V2.1 data analysis software supplied by the VG ESCA-Lab200I-XL instrument manufacturer was used to manipulate the acquired spectra. Transmission electron microscopy (TEM) was performed on a JEOL 2010 TEM equipped with an attachment for local energy dispersion analysis (EDX). The accelerating voltage was 200 kV, and the spot size was 1 nm. High-angle annular dark field scanning transmission microscopy (HAADF-STEM) was performed on the mesoporous Nb–Zr mixed oxide with JEOL JEM-2100F microscope in a scanning transmission electron microscopy (STEM) mode operated at 200 kV. The NH_3 temperature programmed desorption (NH_3-TPD) experiments were carried out using a Autochem 2910 (Micromeritics) surface analyzer quipped with a TCD detector.

2.4 Catalytic reactions

Furfural was converted into 5-hydroxy-2(5*H*)-furanone (HFO) through photocatalytic oxidation with rose bengal. This method has been reported by Gollnick, K.[25] A solution consisting of furfural (18.5 ml, 0.223 mol) and rose bengal (0.455 g) in methanol (115 ml) was bubbled oxygen gas and the mixed solution was irradiated Ace medium-pressure Hg lamp (PLS-LAM500, 500 W, PerfectLight. Crop.) in Pyrex photochemical reactor for 15 h. The as-synthesized 5-hydroxy-2(5*H*)-furanone was recrystallized in chloroform (yield: 85.0%).

The catalytic transformation of 5-hydroxy-2(5*H*)-furanone (HFO) into γ-butyrolactone was carried out in a 100 ml stainless autoclave equipped with a pressure gauge, a magnetic stirrer, and an electric temperature controller. The catalyst (50 mg), dioxane (5 ml) and HFO (0.5 g) were introduced into the autoclave, which then underwent several cycles of flushing with H_2 flow to drive off the air in the autoclave. After pressurizing with H_2 to 5.0 MPa, the reactor was heated to a certain temperature under stirring for several hours. At the end of reaction, the autoclave was cooled to ambient temperature and slowly depressurized. The conversion and product composition were analyzed by GC and GC-MS and chlorobenzene was used as an external standard. GC was performed on a GC-2014 (SHIMADZU) equipped with a high-temperature capillary column (MXT-1, 30 m, 0.25 mm ID) and a FID detector. GC-MS was performed on a GCT Premier/Waters instrument equipped with a capillary column (DB-5MS/J&W Scientific, 30 m, 0.25 mm ID). Identification of main products was based on GC-MS as well as by comparison with authentic samples. The product distribution was shown on the mole basis.

3. Results and discussion

3.1 Physicochemical properties of mesoporous solid acid catalysts

Two structure-directing agents (P123 and F127) are attempted to prepare mesoporous solid acids. As revealed in Fig. 1, F127 is a more efficient template molecule than P123 to fabricate mesoporous Nb–Zr mixed oxides. The sample from P123 shows a weak peak around 1°. However, the materials based on F127 exhibit well-ordered mesostructures. Therefore, F127 was chosed as soft template for further investigations. As shown by the small-angle powder X-ray diffraction patterns (SXRD), there is a strong peak around 0.9°, which is indexed as (100) reflection of the two-dimensional (2D) (*P6mm*) hexagonal mesostructure. Another peak appears around 1.4–1.7°, which reveals the present of long-range ordered mesostructures in these composite oxides.[26,27] The wide-angle X-ray diffraction (WXRD) patterns of the as-prepared mesoporous oxides are shown in Fig. S1.† When the Zr content is between 0 and 40 mol%, these samples exhibited two broad peaks in the 2θ range of 20–40° and 40–65°, indicating that these mesoporous oxides mainly exist in amorphous states. The diffraction lines of tetragonal ZrO_2 were observed at $2\theta = 30.2°$ and 50.2° in the Nb_5Zr_5-550 (PDF#50–1089).

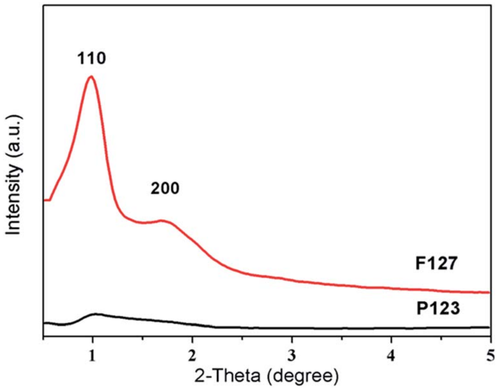

Fig. 1 Small-angle XRD patterns of Nb_5Zr_5-550 sample by using different templates.

The chemical composition of mesoporous Nb–Zr mixed oxides shows many influences on their porosity properties. It is difficult for pure niobium oxide to prepare mesoporous structures through EISA. The presence of zirconium facilitates development of mesoporous structures (Fig. 2a). Nitrogen adsorption–desorption isotherms exhibit type-IV curves (Fig. 2b). There are hysteresis loops at relative pressure (p/p^0) of 0.6–0.9, which are attributed to capillary condensation within the mesopore structure. Pure niobium oxide shows no character of the mesopore structure. Nb_5Zr_5-550 sample has the highest BET surface area (206.4 $m^2\ g^{-1}$). According to BJH analysis, these composite oxides showed uniform-sized mesopores. The average pore diameter changes from 12.2 nm to 5.6 nm with the increase of the Zr proportion (Fig. 2c). As shown in the TEM images (Fig. 3), $Nb_{10-x}Zr_x$-550 (x = 1–5) materials show hexagonally ordered mesoporous structures. These results are consistent with their SXRD patterns and nitrogen adsorption–desorption isotherms. However, pure niobium oxide sample shows a disordered wormhole-like structure (Fig. 3f).

Table 1 summarizes porosity properties of $Nb_{10-x}Zr_x$-550 samples. The average pore sizes of Nb–Zr mixed oxides decrease after Zr incorporation, but the specific surface area values increase with the addition of zirconium. The presence of zirconia is beneficial for maintaining the mesoporous framework. Kondo *et al.* has reported that mesoporous $Zr_6Nb_2O_{17}$ was prepared using P123 as template, the BET surface area of this material was 178 $m^2\ g^{-1}$ at 350 °C calcination temperature and then substantially decreased to 58 $m^2\ g^{-1}$ at 720 °C calcination temperature.[28] STEM and EDS analysis is used to investigate the elemental composition and the distribution of the elements in the mixed oxide. As shown in Fig. 4, the element mapping of the Nb and Zr reveals that niobium and zirconium are homogeneously distributed in the mesoporous frameworks. According to the energy dispersive X-ray spectroscopy (EDS), the atomic ratio of Nb to Zr is 1.06, which is consistent with ICP data.

The characterization of acid catalysts with NH_3-TPD analysis gives an estimation of the total acidity and strength in gas phase. NH_3-TPD curves can be roughly divided into four regions (Fig. 5). The low temperature region from 100 to 350 °C is usually attributed to weak acidic sites. The second region in the range of 350 to 450 °C can be appointed as medium strong acidic sites, and the region of 450–600 °C can be assigned to strong acidic sites. The weak peak around 700 °C might be caused by NH_3 desorption from superacid sites. The total acidity per gram of catalyst gives the following order: Nb_5Zr_5-450 (0.61 $mmol\ g^{-1}$) > Nb_5Zr_5-550 (0.52 $mmol\ g^{-1}$) > Nb_7Zr_3-550 (0.35 $mmol\ g^{-1}$) > Nb-550 (0.11 $mmol\ g^{-1}$). Compared with pure niobium oxide, the mesoporous Nb–Zr mixed oxides contain

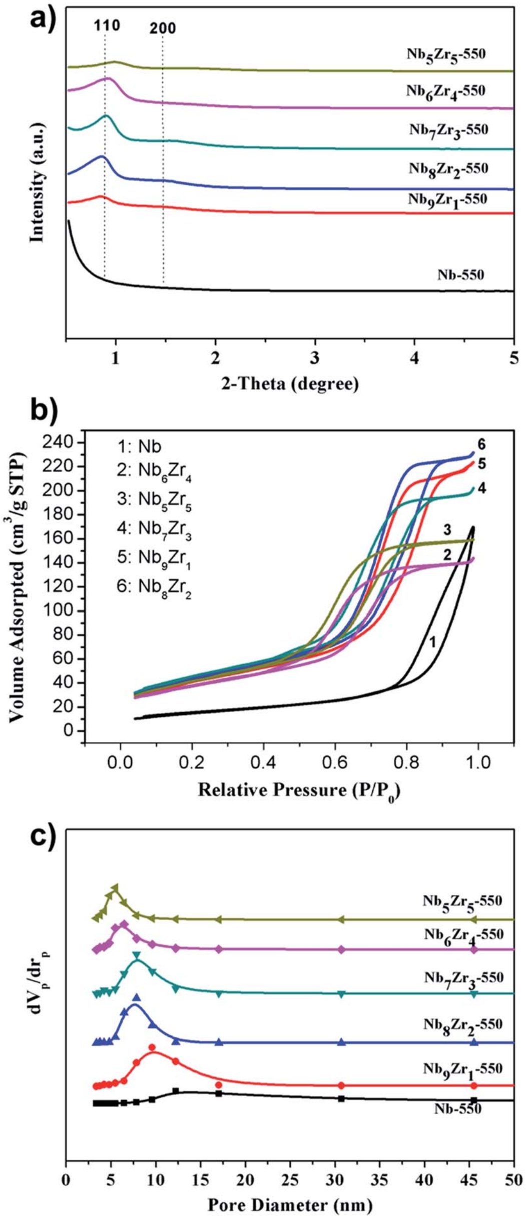

Fig. 2 (a) Small-angle XRD patterns of $Nb_{10-x}Zr_x$-550 samples with different ratio of niobium to zirconium using F127. (b) N_2 sorption isotherms of the $Nb_{10-x}Zr_x$-550 samples using F127. (c) Pore size distribution curves of the $Nb_{10-x}Zr_x$-550 samples using F127.

more weak and strong acid sites. It has been suggested that the formation of M_1-O-M_2 hetero-linkages in binary complex oxides can lead to the non-uniformity of the charge distribution due to the difference for electro negativity and subsequently generate new acid sites.[29] Moreover, the total acidity increases upon zirconia incorporation is in line with the increase of BET surface area except Nb_5Zr_5-450. Although Nb_5Zr_5-450 contains higher amount of the surface acid sites than Nb_5Zr_5-550, higher calcination temperature will lead to removing the weak acid sites. It has been reported that the decrease of acid sites and acid strength upon increasing calcination temperature was observed in mesoporous Ti–W oxides and Nb_2O_5 catalysts.[30,31]

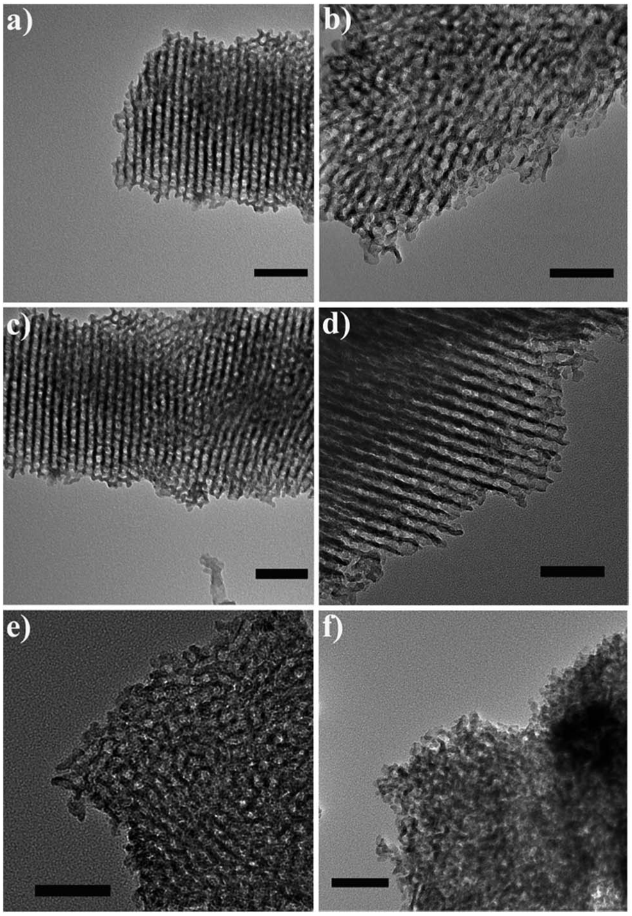

Fig. 3 TEM images of the mesoporous $Nb_{10-x}Zr_x$-550 samples using F127: (a) Nb_5Zr_5, (b) Nb_6Zr_4, (c) Nb_7Zr_3, (d) Nb_8Zr_2, (e) Nb_9Zr_1, (f) Nb (scale bar: 50 nm).

The precursors of metal nanoparticles are introduced by a wet impregnation and supporting catalysts are reduced under diluted hydrogen flow. Fig. 6a shows the HRTEM image of supported Pt nanoparticles. The lattice spaces of the Pt nanoparticles are 0.229 nm and 0.198 nm, which corresponds to the (111) and (200) planes of Pt crystal. X-ray photoemission spectroscopy (XPS) measurement is performed to investigate the surface chemical composition and chemical states. The XPS survey spectrum of the supporting catalyst reveals the presence of carbon, zirconium, niobium, platinum and oxygen (Fig. 6b). The binding energies of Nb $3d_{5/2}$ and $3d_{3/2}$ were 207.3 eV and 210.0 eV, which are indexed to Nb_2O_5 (Fig. S2b†).[32] The Zr 3d XPS spectrum shows two peaks of 182.4 eV ($3d_{5/2}$) and 184.8 eV ($3d_{3/2}$) (Fig. S2a†). This indicates Zr species are in Zr(IV) oxidation state.[33] The insert of Fig. 6b shows Pt 4f peaks. The binding energy of Pt $4f_{7/2}$ is around 70.7 eV and Pt $4f_{5/2}$ is at 74.0 eV, which is indexed to zero-valent platinum species.

3.2 Catalytic performance in sustainable production of γ-butyrolactone from a renewable feedstock molecule

Furfural is converted into 5-hydroxy-2(5*H*)-furanone (HFO) through photocatalytic oxidation and subsequently HFO is

Table 1 Porosity properties of the $Nb_{10-x}Zr_x$-550 samples using F127

	SXRD	Nitrogen adsorption and desorption data			
Samples	2θ (°)	d-spacing (100)[a] (nm)	Specific surface area[b] ($m^2\ g^{-1}$)	Pore size[c] (nm)	Pore volume[d] ($cm^3\ g^{-1}$)
Nb-550	—	—	60.0	12.21	0.27
Nb_9Zr_1-550	0.84	10.53	184.2	7.88	0.36
Nb_8Zr_2-550	0.86	10.22	190.9	7.87	0.38
Nb_7Zr_3-550	0.89	9.91	190.5	6.57	0.33
Nb_6Zr_4-550	0.91	9.63	161.6	5.66	0.23
Nb_5Zr_5-550	0.98	8.95	206.4	5.61	0.30
Nb_5Zr_5-450	1.01	8.66	156.9	4.88	0.19

[a] d-spacing is calculated from the (100) diffraction peak in small-angle XRD patterns. [b] Surface area is calculated by the Brunauer–Emmett–Teller (BET) method. [c] Total pore volume (V_p) is determined by using the adsorption branch of the N_2 isotherm at $P/P^0 = 0.99$. [d] Average pore diameter (D_p) is determined from the local maximum of the BJH distribution of pore diameters obtained in the adsorption branch of the N_2 isotherm.

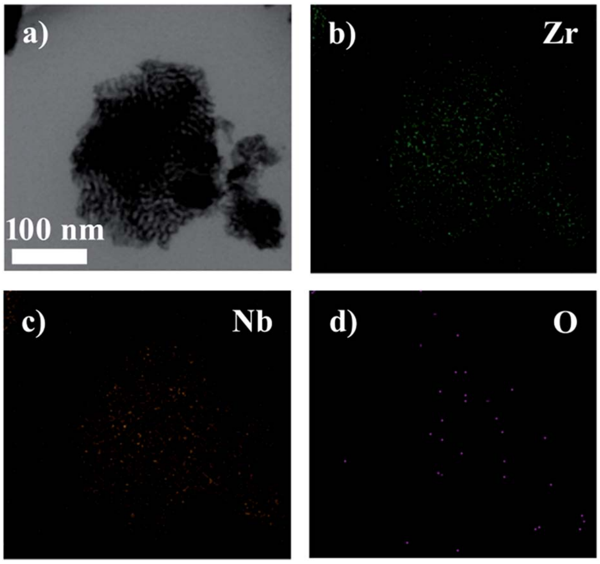

Fig. 4 HAADF-STEM image (a) and the corresponding elemental mapping images of the mesoporous Nb_5Zr_5-550 sample using F127: (b) elemental mapping of Zr; (c) elemental mapping of Nb; (d) elemental mapping of O (scale bar: 100 nm).

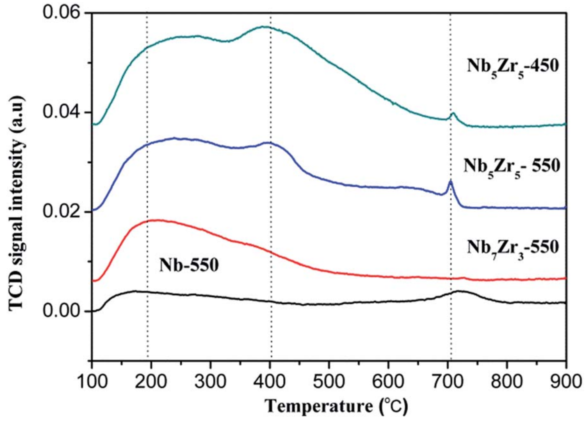

Fig. 5 NH_3-TPD curves of $Nb_{10-x}Zr_x$ mixed oxides using F127.

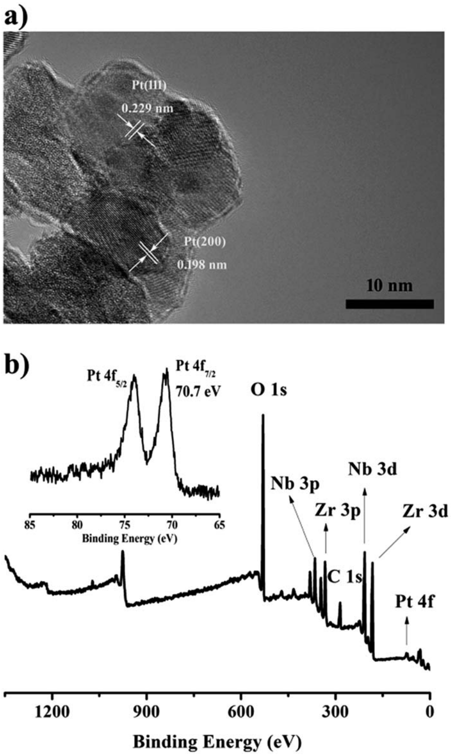

Fig. 6 (a) TEM image of Pt/Nb_5Zr_5-550 catalyst. (b) XPS survey spectrum of Pt/Nb_5Zr_5-550 catalyst (the insert is Pt XPS peaks).

converted into GBL (Scheme 1). There are two types of reactions during conversion of HFO to GBL: hydrogenation and dehydration. Supported Group VIII metal nanoparticles act as the catalytic active sites for hydrogenation, and mesoporous solid acids have two functions: the catalyst support and acidic catalytic sites for dehydration. Based on this bifunctional catalytic surface, these reactions are integrated over one catalyst through one-pot model. Screening experiment results about catalytic activity are summarized in Table 2. Various active metals are tested for HFO conversion. M/Nb_5Zr_5-550 catalysts (M = Ru, Pd, Pt, Rh, Ir) have been investigated under typical reaction conditions (entry 2–6 in Table 2). Supported Ru and Rh catalysts have excellent selectivity of GBL (100%). However, the HFO conversions are relatively low (52.2% and 36.2%). Pd/Nb_5Zr_5-550 and Ir/Nb_5Zr_5-550 catalysts show middle catalytic performances. Pt/Nb_5Zr_5-550 is the best catalyst and GBL yield reached 97.3%.

The compositions of Nb–Zr mixed oxides can exert influences on the catalytic performances. Nb_5Zr_5-550 was tested as the blank sample and it shows no activity (entry 1 in Table 2). Pt/Nb-550 achieved the 91.3% selectivity of GBL with full conversion of HFO. The main by-product was tetrahydrofuran (selectivity: 8.7%). After the introduction of Zirconia into support, the GBL selectivity increased with the percentage of ZrO_2 in the mixed oxides. Pt/Nb_5Zr_5-550 exhibited excellent performance. The selectivity of GBL reached 97.3% under the total conversion of HFO. According to NH_3-TPD analysis, the total acidity of the mixed oxide increases with the ZrO_2 content. These results indicate that the acid properties of support are beneficial to improve the catalytic selectivity. Pt/Nb_5Zr_5-450 gave a high selectivity of HFO, but the HFO conversion decreased to 95.7%. Although Nb_5Zr_5-450 has higher total acidity than Nb_5Zr_5-550, the BET surface area of the former is smaller than that of the latter. High BET surface area facilitates the mass transportation. Several commercial hydrogenation catalysts were tested for HFO conversion. Pd/C and Rh/C showed low performances for HFO conversion, and the GBL yield were 58.1% and 23.8% (Table 3). Pt/C gave the 100% selectivity of GBL with the HFO conversion of 58.6%. Pt/H-ZSM-5 also showed the excellent selectivity of GBL, but the conversion was 60.2%. It is worth noting that the Pt supported on the mesoporous Nb–Zr mixed oxides showed much higher catalytic activity than the conventional platinum catalyst supported on H-ZSM-5. Therefore, Pt/Nb_5Zr_5-550 showed superior catalytic performance in this reaction.

GBL production from HFO involves multi-step consecutive reactions. The GBL formation is attributed to the cooperative effects between active metal and acidic sites. Supported Pt species catalyze the hydrogenation of C=C bond of HFO and 5-hydroxydihydrofuran-2(3*H*)-one (HDFO) is formed (Scheme 1).

Table 2 Screening experimental results of catalytic conversion of HFO to GBL

			Selectivity (%)	
Entry[a]	Catalyst	Conversion (%)	GBL	Others
1	Nb_5Zr_5-550	—	—	—
2	Ru/Nb_5Zr_5-550	52.2	100	—
3	Pd/Nb_5Zr_5-550	73.4	96.7	3.3
4	Ir/Nb_5Zr_5-550	63.7	95.7	4.3
5	Rh/Nb_5Zr_5-550	36.2	100	—
6	Pt/Nb_5Zr_5-550	100	97.3	2.7
7	Pt/Nb_7Zr_3-550	100	95.7	4.3
8	Pt/Nb-550	100	91.3	8.7
9	Pt/Nb_5Zr_5-450	95.7	97.7	2.3

[a] Reaction condition: 0.5 g HFO, 50 mg catalyst, 5 ml dioxane, 5 MPa H_2, 140 °C/8 h.

Table 3 Results of the conversion of HFO over hydrogenation catalysts

			Selectivity (%)	
Entry[a]	Catalyst[b]	Conversion (%)	GBL	Others
1	Rh(5 wt%)/C	23.8	100	—
2	Pt(5 wt%)/C	58.6	100	—
3	Pd(10 wt%)/C	60.8	95.5	4.5
4	Pt(2 wt%)/HZSM-5	60.2	100	—
5	Pt(2 wt%)/Nb_5Zr_5-550	100	97.3	2.7

[a] Reaction condition: 0.5 g HFO, certain amount of catalyst, 5 ml dioxane, 5 MPa H_2, 140 °C/8 h. [b] The used amount of active metal in different catalyst was similar.

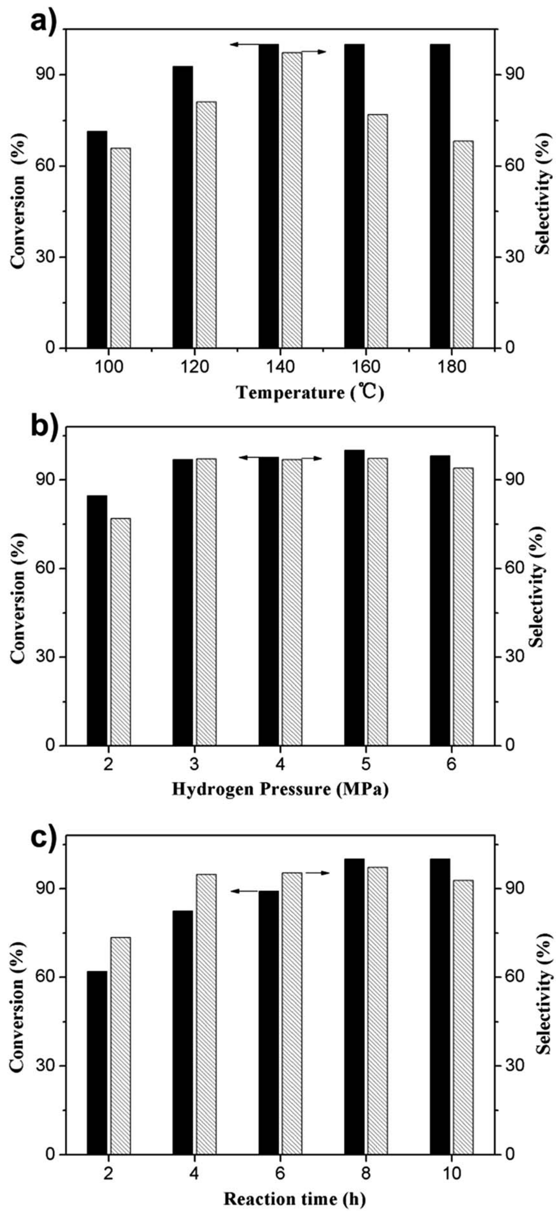

Fig. 7 (a) The effects of reaction temperature on HFO conversion and GBL selectivity. (b) HFO conversion and GBL selectivity related to the elevation of hydrogen pressure. (c) The effects of reaction time on HFO conversion and GBL selectivity.

GBL from HDFO proceeds *via* dehydration catalyzed by acid sites of mesoporous solid acid sites and subsequent hydrogenation of double carbon bonds over supported Pt nanoparticles. During these processes, the main by-products are THF and butyric acid, which are resulted from further hydrogenation of GBL. Excellent GBL selectivity reveals that the side reactions are inhibited over the metal–acid bifunctional catalyst through selecting proper acidic support and active metals.

The reaction condition was further optimized with Pt/Nb_5Zr_5-550. The effects of reaction temperature on HFO conversion are investigated from 100 °C to 180 °C (Fig. 7a). HFO conversion increases from 100 °C to 140 °C and further elevation of temperature shows little influence. Higher reaction temperature (180 °C) directly leads to the drop of GBL yield. GBL can be further converted to saturated compound or ring-opening product under high temperature, such as THF and butyric acid. Tetrahydrofuran and 1,4-butanediol have been detected in the catalytic hydrogenation of succinic acid to GBL with Pd/TiO_2 or Re/MC-X catalysts.[9,34]

HFO conversions and GBL selectivity are found to increase with the elevation of hydrogen pressure from 2 to 5 MPa (Fig. 7b). Further elevation in reaction pressure is detrimental to the catalytic activity and selectivity. This might be ascribed to the degradation of GBL to THF or butyric acid at a higher reaction pressure. The best performance is achieved under hydrogen pressure of 5.0 MPa and the GBL yield reaches 97.3%. When the reaction time increases from 2 h to 8 h, the conversion increase sharply from 61.9% to 100% and the selectivity rises from 73.4% to 97.3% (Fig. 7c). Over-hydrogenation is observed with the prolonged reaction time. HDFO is prone to take ring-opening in the protic solvents, such as alcohol or H_2O. Aprotic solvents (dioxane or THF) are selected as reaction medium. When THF is used as solvent, the GBL selectivity is only 67.9% with full conversion of HFO. Butyric acid is detected with the selectivity of 32.1%.

4. Conclusions

In summary, we developed a sustainable strategy for GBL production from renewable biomass-based furfural, which involves photocatalytic oxidation of furfural into 5-hydroxy-2(5*H*)-furanone (HFO) and subsequent hydrodeoxygenation of HFO into GBL. The hydrodeoxygenation reaction was carried out using Pt catalyst supported on mesoporous Nb–Zr mixed metal oxides. The as-synthesized mixed oxides have ordered mesostructures, large specific surface area, large pore volume and uniform pore size distribution. The resulting bifunctional catalysts exhibited excellent catalytic performance in the hydrodeoxygenation of HFO into GBL. The incorporation of zirconia into support improves the thermal stability of mesoporous mixed oxides and increases the surface acid amounts, which contribute to catalytic selectivity. Pt/Nb_5Zr_5-550 exhibited the best catalytic performances with 97.3% selectivity of GBL at full conversion. The excellent performance can be correlated with the cooperative effect between active metal and acid sites. An overall GBL yield of 82.7% from furfural was obtained. This work provides a novel and eco-friendly pathway to produce high valued-added γ-butyrolactone from renewable resources.

Acknowledgements

This work was supported by the National Natural Science Foundation of China (NSFC, No. 21403248; 21174148, 21101161).

Notes and references

1 Y. L. Zhu, J. Yang, G. Q. Dong, H. Y. Zheng, H. H. Zhang, H. W. Xiang and Y. W. Li, *Appl. Catal., B*, 2005, **57**, 183–190.
2 M. Seitz and O. Reiser, *Curr. Opin. Chem. Biol.*, 2005, **9**, 285–292.
3 J. Huang, W. L. Dai, H. X. Li and K. N. Fan, *J. Catal.*, 2007, **252**, 69–76.
4 Y. Yu, W. C. Zhan, Y. Guo, G. Z. Lu, S. Adjimi and Y. L. Guo, *J. Mol. Catal. A: Chem.*, 2014, **395**, 392–397.
5 M. E. Bertone, C. I. Meyer, S. A. Regenhardt, V. Sebastian, T. F. Garetto and A. J. Marchi, *Appl. Catal., A*, 2015, **503**, 135–146.
6 D. W. Hwang, P. Kashinathan, J. M. Lee, J. H. Lee, U. H. Lee, J. S. Hwang, Y. K. Hwang and J. S. Chang, *Green Chem.*, 2011, **13**, 1672–1675.
7 C. Aellig, F. Jenny, D. Scholz, P. Wolf, I. Giovinazzo, F. Kollhoff and I. Hermans, *Catal. Sci. Technol.*, 2014, **4**, 2326–2331.
8 B. Tapin, F. Epron, C. Especel, B. K. Ly, C. Pinel and M. Besson, *ACS Catal.*, 2013, **3**, 2327–2335.
9 K. H. Kang, U. G. Hong, J. O. Jun, J. H. Song, Y. Bang, J. H. Choi, S. J. Han and I. K. Song, *J. Mol. Catal. A: Chem.*, 2014, **395**, 234–242.
10 Z. F. Shao, C. Li, X. Di, Z. H. Xiao and C. H. Liang, *Ind. Eng. Chem. Res.*, 2014, **53**, 9638–9645.
11 G. Q. Ding, Y. L. Zhu, H. Y. Zheng, W. Zhang and Y. W. Li, *Catal. Commun.*, 2010, **11**, 1120–1124.
12 A. Corma, S. Iborra and A. Velty, *Chem. Rev.*, 2007, **107**, 2411–2502.
13 T. Mizugaki, T. Yamakawa, Y. Nagatsu, Z. Maeno, T. Mitsudome, K. Jitsukawa and K. Kaneda, *ACS Sustainable Chem. Eng.*, 2014, **2**, 2243–2247.
14 P. Li and H. Alper, *J. Mol. Catal.*, 1992, **72**, 143–152.
15 M. Sommovigo and H. Alper, *J. Mol. Catal.*, 1994, **88**, 151–158.
16 L. Metsger and S. Bittner, *Tetrahedron*, 2000, **56**, 1905–1910.
17 M. Salavati-Niasari, *Inorg. Chem. Commun.*, 2006, **9**, 628–633.
18 A. Ausavasukhi and T. Sooknoi, *Green Chem.*, 2015, **17**, 435–441.
19 S. Shi, H. J. Guo and G. C. Yin, *Catal. Commun.*, 2011, **12**, 731–733.
20 J. H. Lan, Z. Q. Chen, J. C. Lin and G. C. Yin, *Green Chem.*, 2014, **16**, 4351–4358.
21 H. Choudhary, S. Nishimura and K. Ebitani, *Appl. Catal., A*, 2013, **458**, 55–62.
22 N. Alonso-Fagundez, I. Agirrezabal-Telleria, P. L. Arias, J. L. G. Fierro, R. Mariscal and M. L. Granados, *RSC Adv.*, 2014, **4**, 54960–54972.
23 N. Alonso-Fagulndez, M. L. Granados, R. Mariscal and M. Ojeda, *ChemSusChem*, 2012, **5**, 1984–1990.

24 S. B. Liu, Y. Amada, M. Tamura, Y. Nakagawa and K. Tomishige, *Green Chem.*, 2014, **16**, 617–626.

25 K. Gollnick and A. Griesbeck, *Tetrahedron*, 1985, **41**, 2057–2068.

26 P. D. Yang, D. Y. Zhao, D. I. Margolese, B. F. Chmelka and G. D. Stucky, *Nature*, 1998, **396**, 152–155.

27 B. Lee, D. L. Lu, J. N. Kondo and K. Domen, *J. Am. Chem. Soc.*, 2002, **124**, 11256–11257.

28 D. L. Lu, B. Lee, J. N. Kondo and K. Domen, *Microporous Mesoporous Mater.*, 2004, **75**, 203–208.

29 Q. Zhang, Y. Zhang, H. T. Li, C. G. Gao and Y. X. Zhao, *Appl. Catal., A*, 2013, **466**, 233–239.

30 Y. H. Zhang, X. C. Zhao, Y. Wang, L. K. Zhou, J. Y. Zhang, J. Wang, A. Q. Wang and T. Zhang, *J. Mater. Chem. A*, 2013, **1**, 3724–3732.

31 F. Wang, H. Z. Wu, C. L. Liu, R. Z. Yang and W. S. Dong, *Carbohydr. Res.*, 2013, **368**, 78–83.

32 C. García-Sancho, R. Moreno-Tost, J. M. Mérida-Robles, J. Santamaría-González, A. Jiménez-López and P. Maireles-Torres, *Appl. Catal., B*, 2011, **108**, 161–167.

33 R. Kourieh, S. Bennici, M. Marzo, A. Gervasini and A. Auroux, *Catal. Commun.*, 2012, **19**, 119–126.

34 U. G. Hong, H. W. Park, J. Lee, S. Hwang, J. Yi and I. K. Song, *Appl. Catal., A*, 2012, **415**, 141–148.